AIAA AVIATION Forum
August 2-6, 2021, VIRTUAL EVENT
AIAA AVIATION 2021 FORUM

10.2514/6.2021-2831

Aero-Optical Measurements of a Mach 8 Boundary Layer

Kyle P. Lynch[1], Russell Spillers[2], Nathan E. Miller[3], Daniel R. Guildenbecher[4]
Sandia National Laboratories
Albuquerque, New Mexico 87123

Stanislav Gordeyev[5]
Department of Aerospace and Mechanical Engineering,
University of Notre Dame, Notre Dame, Indiana 46545

Measurements are presented of the aero-optic distortion produced by a Mach 8 turbulent boundary layer in the Sandia Hypersonic Wind Tunnel. Flat optical inserts installed in the test section walls enabled a double-pass arrangement of a collimated laser beam. The distortion of this beam was imaged by a high-speed Shack-Hartmann sensor at a sampling rate of up to 1 MHz. Analysis is performed using two processing methods to extract the aero-optic distortion from the data. A novel de-aliasing algorithm is proposed to extract convective-only spectra and is demonstrated to correctly quantify the physical spectra even in case of relatively low sampling rates. The results are compared with an existing theoretical model, and it is shown that this model under-predicts the experimentally measured distortions regardless of the processing method used. Possible explanations for this discrepancy are presented. The presented results represent to-date the highest Mach number for which aero-optic boundary layer distortion measurements are available.

I. Introduction

Aero-optical distortions are caused by the dependence of the index of refraction, n, on the gas phase density, ρ. This is described by the Gladstone-Dale relation, $n - 1 = \rho K_{GD}$, where K_{GD} is the Gladstone-Dale constant. For air near ambient temperatures and visible wavelengths, $K_{GD} \approx 2.27 \times 10^4$ m^3/kg [1]. Light passing through a region of flow with varying density will therefore be distorted due to the varying index of refraction field. This distortion is typically quantified by the optical path difference (OPD), defined as the line-of-sight integral of the fluctuating index of refraction,

$$OPD(x,y,t) = \int n'(x,y,z,t)\, dz = K_{GD} \int \rho'(x,y,z,t)\, dz \tag{1}$$

The aero-optical phenomena occurring in subsonic and low-supersonic flows are well established [2]; however, there are fewer studies quantifying these phenomena at hypersonic speeds. Wyckham and Smits [3] performed measurements at transonic speeds and at approximately Mach 7.7 using a 2-D wavefront sensor. They showed that large-scale motions on the order of the boundary layer thickness dominated the measured distortions and proposed a wavefront distortion scaling based on the bulk flow. Subsequently, Gordeyev et al. [4] proposed a double-pass measurement for subsonic boundary layers and were able to measure convective speeds of aero-optic structures,

[1] Senior Member of Technical Staff, Aerosciences Department, AIAA Senior Member. Corresponding author: klynch@sandia.gov
[2] Principal Technologist, Aerosciences Department, AIAA Member.
[3] Senior Member of Technical Staff, Aerosciences Department, AIAA Member.
[4] Principal Member of Technical Staff, Diagnostic Science and Engineering Department. AIAA Senior Member.
[5] Associate Professor, Department of Aerospace and Mechanical Engineering. AIAA Associate Fellow.

deflection angle spectra, and the root mean square optical path difference, OPD_{rms}. Using the Strong Reynolds Analogy (SRA), Gordeyev et al. [4, 5] further proposed an analytical model to predict these aero-optical distortions and demonstrated that the model adequately predicts the observed values of OPD_{rms}. These techniques were extended to Mach 3.0 and 4.3 by Gordeyev et al. [6], and to the hypersonic regime in the Boeing/AFOSR Mach 6 Quiet Tunnel by Gordeyev and Juliano [7, 8]. These high Mach tests showed that the measured OPD_{rms} values become consistently larger than predicted by the existing model for lower speed flat-plate turbulent boundary layers. Further, they conjectured that the assumptions underlying this model, originally developed for subsonic and low-supersonic boundary layers, become increasingly invalid in the hypersonic regime.

Several other experimental hypersonic aero-optic studies exist in the literature, but do not explicitly quantify the distortions caused by the boundary layer. In Winter et al. [9], direct image distortion measurements were performed using image calibration targets, but quantitative wavefront measurements were not performed. Lee et al. [10] present experiments performed in a reflected shock tunnel with an internally mounted wavefront sensor in a wedge model. Mean tilt, boresight error, and Strehl ratio were measured, but the OPD_{rms} distortion was not reported.

The objective of this work is to extend the measurements performed in [7] to a higher Mach number, and use these measurements to evaluate the efficacy of an existing aero-optics model. In section II, the experimental setup, flow conditions, and data processing steps are detailed. In section III, the aero-optics results are reported and compared to the model, and a discussion is presented over the findings.

II. Experimental Campaign

A. Wind Tunnel Facility

The Sandia Hypersonic Wind Tunnel (HWT) is a conventional blowdown-to-vacuum facility with interchangeable nozzles for Mach 5, 8, or 14 operation. Typical runtimes are on the order of 30 sec. The Mach 8 (HWT-8) capability is used for all tests herein. HWT-8 uses high-pressure nitrogen as a test gas, with a stagnation pressure P_0 and temperature T_0 range from 1.7-6.9 MPa and 500-890K, respectively. The test section is circular with a diameter of 35.6 cm. The freestream noise levels have been previously estimated between 3-5% using pressure measurements [11]. The specific test conditions approximately match the Mach 7.9 case of Smith et al. [12], with P_0 = 4.7 MPa and T_0 = 620 K. Isentropic relations and Sutherland's law yield an approximate freestream temperature of 45 K, density of 0.04 kg/m^3 and Reynolds number 14.0 × 10^6/m. A CFD simulation of this condition was used to estimate the boundary layer thickness δ and skin friction coefficient C_f at the measurement location to be 40.6 mm and 6.13 x 10^{-4}, respectively. Several runs were performed for repeatability with multiple imaging configurations as shown in Table 1. The tunnel has limited closed-loop control, leading to slight variation in conditions between runs.

Table 1. Summary of dataset

Run	Frame Rate [kHz]	Record Length [sec]	Number of Lenslets	Physical Resolution [mm]	P_0 [MPa]	T_0 [K]	U_∞ [m/s]*	ρ_∞ [kg/m^3]*
2	1000.0	2.4	1 × 62	0.2 × 14.6	4.74 ± 0.03	617 ± 11	1089	0.037
5	1000.0	2.4	1 × 62	0.2 × 14.6	4.78 ± 0.03	622 ± 12	1093	0.037
8	1000.0	2.4	1 × 62	0.2 × 14.6	5.20 ± 0.03	576 ± 14	1052	0.043
4	396.226	1.7	5 × 64	1.0 × 15.1	4.75 ± 0.03	613 ± 11	1085	0.037
7	396.226	1.7	5 × 64	1.0 × 15.1	4.75 ± 0.05	624 ± 12	1095	0.036
10	396.226	1.7	5 × 64	1.0 × 15.1	4.70 ± 0.05	625 ± 11	1096	0.036
3	113.513	1.5	23 × 64	5.3 × 15.1	4.66 ± 0.03	628 ± 11	1098	0.035
6	113.513	1.5	23 × 64	5.3 × 15.1	4.77 ± 0.04	619 ± 12	1091	0.037
9	113.513	1.5	23 × 64	5.3 × 15.1	4.76 ± 0.04	618 ± 12	1090	0.037

*Estimated from isentropic relations and P_0 and T_0 tunnel measurements.

B. Optical Configuration

All measurements were collected using a high-speed Shack-Hartmann wavefront sensor. An optical schematic is shown in Fig. 1. A CW laser source (Coherent Verdi) is launched into a fiber and brought to an optical table beside the wind tunnel. The output of the fiber is collimated using a 250 mm achromat lens and directed into the test section using a 50/50 non-polarizing beamsplitter cube. A pair of flat 25.4 mm BK7 window inserts are used to pass the beam through the test section while minimizing any geometrical step. It is estimated that the maximum streamwise step height is approximately 1 mm, compared to the estimated boundary layer thickness of ~30 mm. These window inserts are the effective aperture of the system.

The beam is reflected by a 0 deg mirror, makes a second pass through the test section along the same path, exits back into the beam splitter, and is then reimaged using a pair of 400 and 500 mm lenses to increase the optical

magnification such that the beam fully fills the active area of the sensor. Finally, the resulting collimated beam is projected onto a custom microlens array (f = 38 mm, pitch = 0.3 mm) and imaged using a Phantom v2511 monochrome high-speed camera. In this setup, the image plane of the camera and lens system is aligned to the location of the 0 deg mirror. The resulting spatial resolution of the deflection angles was $\Delta x = \Delta z = 0.24$ mm.

Multiple imaging rates and fields of view were used to adequately capture convecting turbulence and the spatial characteristics of aberrating flow structures. The former used the maximum camera frame rate of 1 MHz. To operate at this rate, a 16 x 768 pixel region was captured by the sensor. This corresponds to a single row of lenslets. Conversely, to image spatial structures, two larger fields of view were used. In all cases, the frame rate was set to the maximum available for the fields of view, which is lower than the 1-D line. A summary of all runs and relevant experimental conditions are given in Table 1. For each imaging configuration, the total sampling duration during each run is approximately 1.5-2.5 seconds, which was started ~2-3 seconds after the tunnel reached stable flow conditions.

Image processing consists of time-series dot shift estimation using an in-house intensity centroiding code. The corresponding time-averaged values of dot shifts were subtracted from the individual time series to remove stationary distortions. No image pre-processing or intensity corrections are performed. The shifts are then converted to deflection angles based on the geometry of the lenslet array.

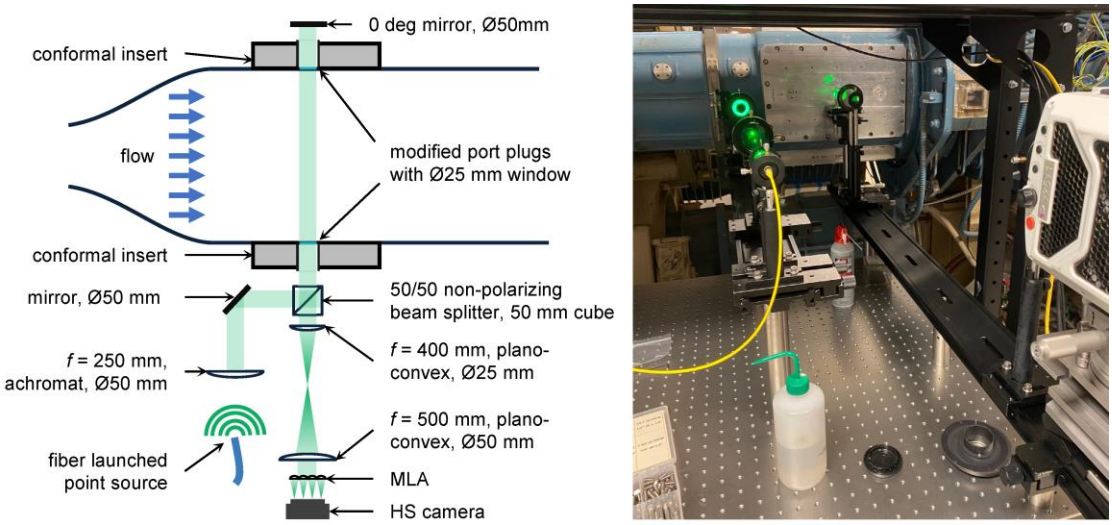

Fig. 1 Left, schematic optical configuration. Right, photo of setup installed by the wind tunnel.

III. Results and Discussion

A. Data Reduction

Before presenting the data reduction, note that the beam propagates through two boundary layers, one on each side of the tunnel. The approach by Gordeyev et al. [4, 5] is adopted where it is assumed that the boundary layers on both sides are statistically the same and independent. Therefore, the statistics of a single boundary layer are extracted from the double boundary layer experiment by dividing the wavefront amplitudes by $\sqrt{2}$.

The goal of these experiments is to extract the magnitude of aero-optical distortions, OPD_{rms}, and the corresponding convective speed, U_c, of the underlying aero-optical structures. The Shack-Hartmann sensor measures deflection angles (θ_x, θ_z) at discrete locations (x, z) over the aperture. The deflection angles are related to the wavefront $W(x, z)$ via the spatial gradient, $\theta_x = \frac{\partial W}{\partial x}$, $\theta_z = \frac{\partial W}{\partial z}$. Therefore, it is possible to reconstruct the wavefront over the aperture from the deflection angles using, e.g., Southwell's method [13].

The resulting reconstructed wavefronts are known up to an arbitrary constant. To make the solution unique, a spatial mean value of the wavefront, called a piston component, at every time instant is forced to zero, $\int_{Ap} W(x, z, t) dx dz = 0$. Further, the wavefront measurements are almost always corrupted by mechanical vibrations, which manifest as an additional unsteady spatial tip/tilt component in the wavefronts, $A(t)x + B(t)z$. A typical practice is to remove tip/tilt components from the instantaneous wavefronts; however, this reduces the overall level of measured aero-optical

distortions. This reduction is often termed the aperture effect in literature [14, 4]. For turbulent boundary layers, if the aperture size Ap, is smaller than the boundary layer thickness, δ, the tip/tilt-removed OPD_{rms} values are reduced by more than 60% for both subsonic and supersonic boundary layers [7]. While in general it is difficult to extract correct aero-optical levels from small aperture data, in some cases it is possible.

An alternative approach can be used if the aero-optical structure primarily convects over the aperture. In this case, Taylor's frozen field hypothesis can be used to approximate the spatial derivatives via temporal derivatives, $\frac{\partial W}{\partial x} = \frac{1}{U_C}\frac{\partial W}{\partial t} = \theta_x$ [4]. This can be integrated in time if the time-series of the deflection angles and the convective speed are known. Applying a Fourier Transform yields $\frac{i\omega}{U_C}\widehat{W} = \hat{\theta}_x$, which provides a useful relation between the autospectral density functions of the wavefront, $S_w(f)$, and the streamwise deflection angle, $S_\theta(f)$ [4],

$$S_W(f) = \left(\frac{U_C}{2\pi f}\right)^2 S_\theta(f) \tag{2}$$

In many cases, the spectral form is more advantageous, as it allows various filters to be applied for removal of vibrations, electronic noise, etc. The overall level of aero-optical distortions, OPD_{rms}, can then be calculated from the deflection angle spectrum by integrating over frequency,

$$OPD_{rms}^2 = 2U_C^2 \int_0^\infty \frac{S_\theta(f)}{(2\pi f)^2} df \tag{3}$$

For example, deflection angles from a single line of lenslets, collected at the sampling frequency of 1 MHz, are visualized in the *x-t* plot in Fig. 2. This represents a very short time interval within the total measurement. A prominent feature in the data is the convecting structures which remain coherent over the span of the aperture.

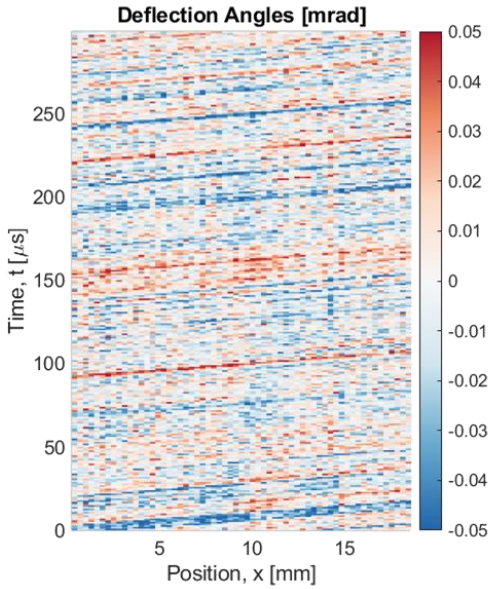

Fig. 2. *x-t* plot of the deflection angles in milliradians for the sampling frequency of 1 MHz.

A dispersion analysis of these deflection angles [4, 15] is effective for characterizing convecting optical disturbances. This approach computes a two-dimensional autospectral density function of the deflection angles $S_\theta(f, k_x)$, as described by Eq. 4. The spectrum is estimated using Welch's method with no block overlap and squared-cosine block weighting following the procedure in Bendat and Piersol [16]. The block size was $[N_t \times N_x]$ points, with N_t = 10,000 temporal points and N_x = 63 spatial points.

$$\hat{\theta}(k_x, f) = \int_0^D \int_0^T \theta(t, x) e^{-j2\pi(ft + k_x x)}\, dt\, dx, \qquad S_\theta(f, k_x) = \frac{\langle \widehat{\theta^*}(k_x, f)\hat{\theta}(k_x, f)\rangle}{T \cdot Ap} \tag{4}$$

Here $T = N/f_s$ is the block duration, N is the block size, $Ap = N_x \times \Delta x$ is the beam aperture in the streamwise direction, and angled brackets denote block averaging. Examples of the autospectral density functions for different sampling frequencies are shown in Fig. 3. The most prominent feature is caused by the traveling structures observed in Fig. 2.; these correspond to lines defined by $2\pi ft - k_x x =$ const. Therefore, traveling structures appear as constant slope branches in the dispersion spectra, where the slope indicates the direction and magnitude of the convecting velocity as $U_c = 2\pi f/k_x$. Another feature of the spectrum is severe aliasing, with additional branches appearing on both sides of the main branch. This spectral aliasing indicates that a direct implementation of Eq. 3 to compute OPD_{rms} will be biased, and it also hinders a two-point spectral cross-correlation technique to compute the convective speed [4].

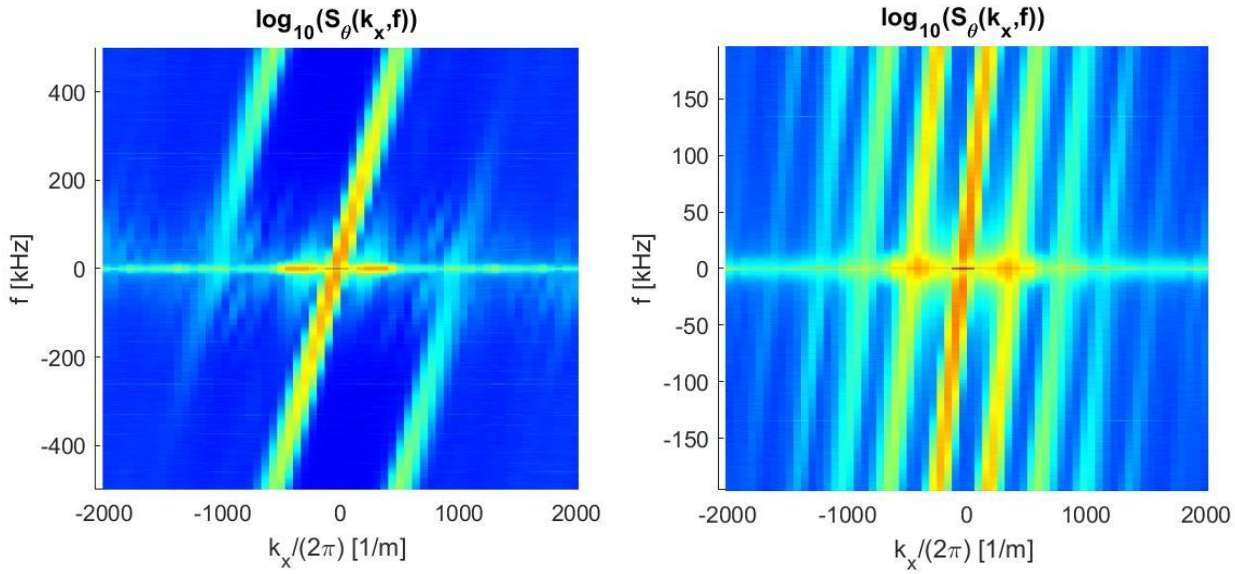

Fig. 3. Two-dimensional spectra of the deflection angles for sampling frequency (a) f_s = 1 MHz and (b) f_s = 393 kHz. For both plots, Δx = 0.24 mm.

To understand the origin of the spurious branches in Fig. 3, consider a purely convective signal. An idealized spectrum for a continuous 2-D Fourier transform (an infinite sampling frequency) is shown schematically in Fig. 4(a) as a single branch with a constant slope, determined by the convective speed. For simplicity, consider aliasing in time only. If the signal is sampled at a finite sampling frequency f_s, the Nyquist–Shannon sampling theorem states that the resulting discrete spectrum will be a superposition of infinite number of continuous spectra, periodically shifted by $n \times f_s$, where n is an integer number, as illustrated in Fig. 4(b). If the original spectrum has frequency content above the Nyquist frequency, $f_s/2$, it will result in shifted branches entering the range of frequencies $[-f_s/2, +f_s/2]$, as shown inside the rectangular box in Fig. 4(a). This is a classic example of aliasing in discrete 2-D Fourier transforms.

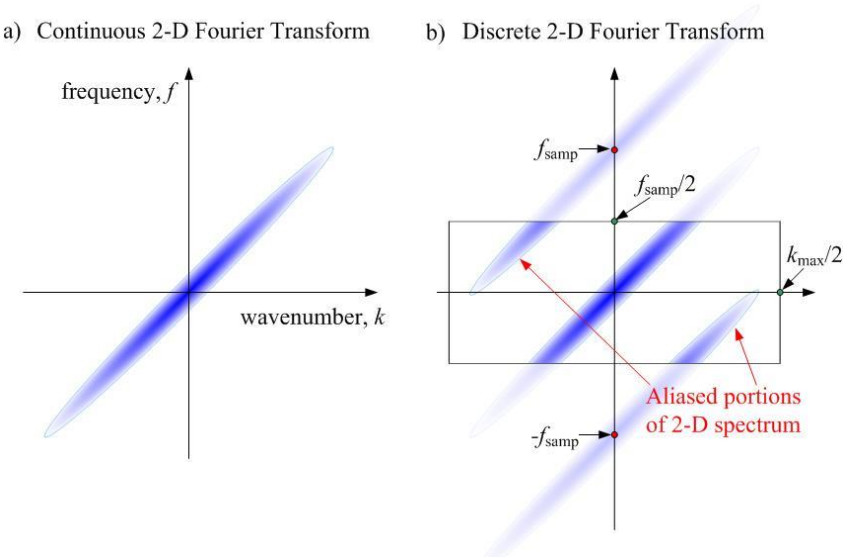

Fig. 4. Schematic illustrating temporal aliasing of convective 2-D spectra with insufficient sampling frequency.

Understanding the origin of the aliasing provides a possible way to remove it. The algorithm is demonstrated in Fig. 5. Consider a discrete 2-D spectrum, aliased in time, as in Fig. 3(a). This can be shifted by $\pm f_s$, $\pm 2f_s$, and so on, and stacked above and below the discrete spectrum, as in Fig. 5(b). This leads to the main branch recovering its original shape. By applying a band filter, shown as a shaded region in Fig. 5(c), the main branch can be isolated and analyzed. Finally, the de-aliased temporal spectrum can be computed by integrating the band-passed 2-D spectrum in the wavenumber space,

$$S_\theta(f) = \frac{1}{2\pi}\int_{-\infty}^{\infty} BandPass\, S_\theta(f, k_x) dk_x \tag{5}$$

By slope fitting the ridge of the main branch, the convective speed U_c can also be computed and OPD_{rms} can be calculated from this de-aliased deflection angle spectrum by applying Eq 3.

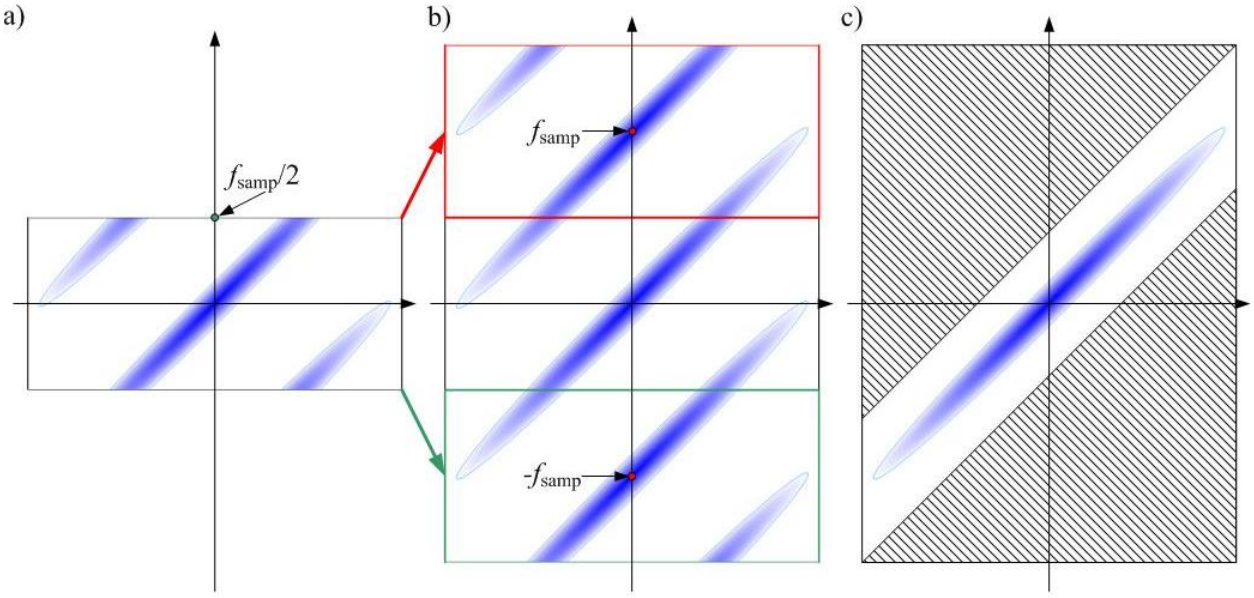

Fig. 5. Schematic illustrating a proposed de-aliasing algorithm to recover the temporal spectrum.

Implementation of the de-aliasing algorithm for the sampling frequency of 1 MHz is shown in Fig. 6. Is this case, stacking the discrete spectrum only once, on top and on bottom, is sufficient to recover the main branch, as demonstrated in Fig. 6(a). Open circles identify the ridge of the main branch and a linear fit was used to compute the convective speed. Applying a band filter and integrating the spectrum in wavenumber space gives the de-aliased spectrum, shown as a red line in Fig. 6(b). For comparison, the deflection angle spectrum from a single point is also plotted in Fig. 6(b) as a blue line. Contamination in the low range of frequencies between 1 kHz and 20 kHz is significantly reduced. More importantly, the de-aliased spectrum is extended up to 1.5 MHz, beyond the Nyquist frequency and even the sampling frequency. The low-end of the spectrum below 1 kHz is still influenced by mechanical vibrations and a digital low-pass filter with a cut-off value f_{cut} = 2.7 kHz is used to remove the vibration-contamination part of the spectrum before computing OPD_{rms}.

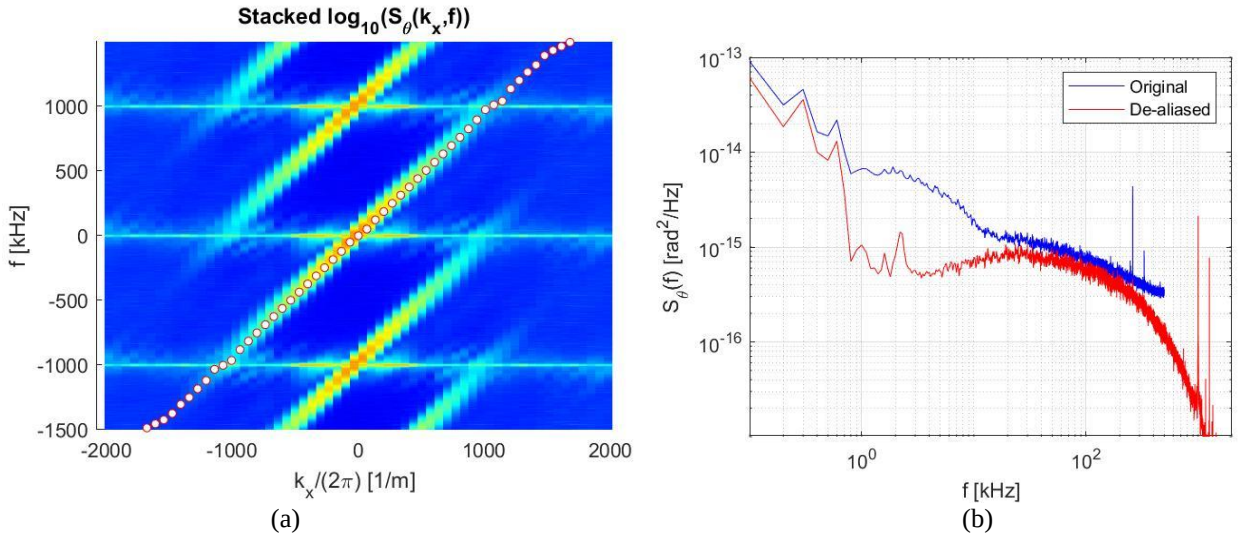

Fig. 6. (a) Stacked 2-D spectrum with the location of the main branch indicated with filled circles. (b) The single-point and de-aliased temporal spectra of the deflection angles. The sampling frequency is f_s = 1 MHz.

Fig. 7 demonstrates that the algorithm works well for even a lower sampling frequency of 393 kHz. In this case, the discrete spectrum was stacked three times above and below to recover the original branch, see Fig. 7(a). The de-aliased and single-point spectra are plotted in Fig. 7(b). While the single-point spectrum is significantly aliased over the whole range of the resolved frequencies, the de-aliased spectrum is similar to the de-aliased spectrum in Fig. 6(b), and also extends well beyond the sampling frequency. These two examples demonstrate that if the imaging and lenslet setup have sufficient spatial resolution and number of spatial points, the corresponding deflection angle spectra can be recovered even for temporally undersampled data. Note, at some lower limit of temporal sampling frequencies, aliased components would tend to overlap, and the techniques presented here would fail. Still, as demonstrated here, widely available high-speed cameras can readily provide sufficient temporal resolution, and the lower limit of sampling frequency has yet to be approached.

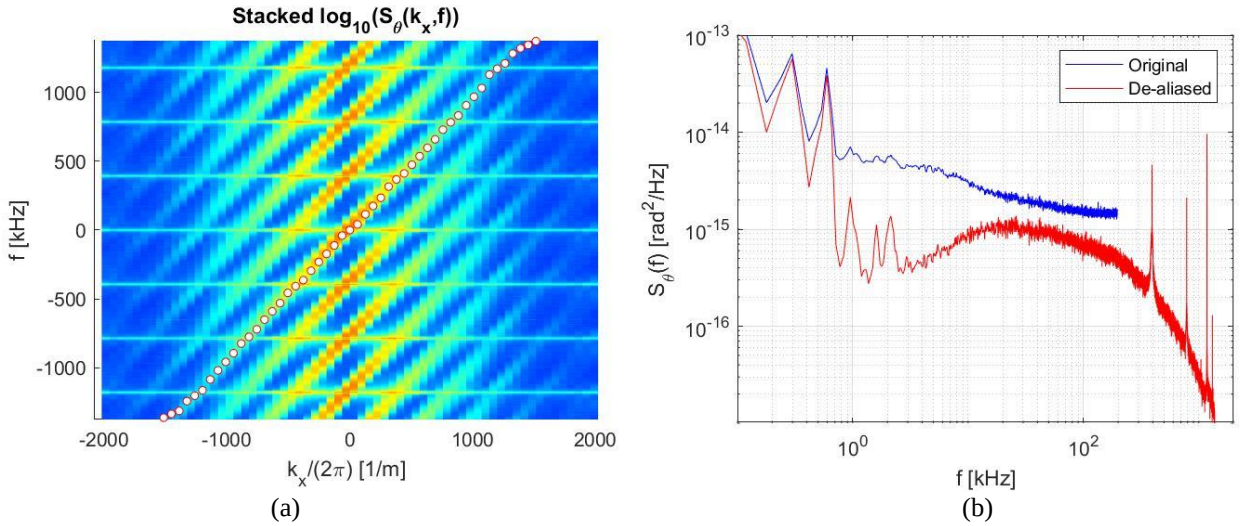

(a) (b)

Fig. 7. (a) Stacked 2-D spectrum with the location of the main branch indicated with filled circles. (b) The single-point and de-aliased temporal spectra of the deflection angles. The sampling frequency is f_s = 393 kHz.

B. Deflection Angles Results

Fig. **8** presents the de-aliased auto-spectral density function for the deflection angle vs normalized frequency, $St_\delta = f\delta/U_\infty$, for the sampling frequency of 1 MHz as a black line. Deflection angle spectra for M = 3, 4.3, and 5.8 from [7] are also plotted for comparison. Except for the vibration-corrupted low frequency components, all spectra approximately collapse into each other for $St_\delta > 0.2$, indicating that the large-scale structure, which is responsible for most of the aero-optical distortions, does not change significantly with the Mach number. The peak in all spectra is at approximately at $St_\delta = 1$, implying that the large-scale structure is on the order of the boundary layer thickness. The fact that the spectral peak location is the same for a wide range of Mach numbers, including the subsonic regime [4], is a useful result. This provides a non-intrusive method to estimate the turbulent boundary layer thickness over a wide range of Mach numbers by simply sending a small-aperture laser beam normal to the boundary layer, measuring the resulting streamwise deflection angles and finding the location of the peak in the deflection angle spectrum.

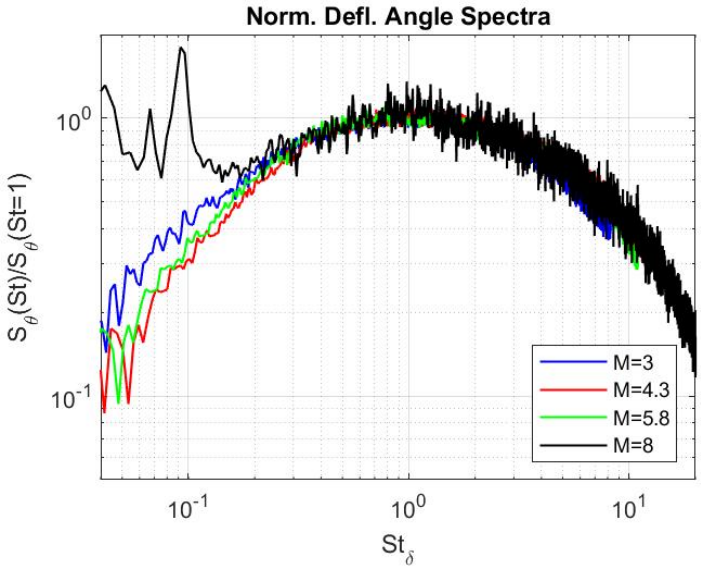

Fig. 8. Deflection angle spectra as a function of , $St_\delta = f\delta/U_\infty$, normalized by the value at St_δ = 1 for M = 3, 4.3 and 5.8 from [7]**, the de-aliased spectrum for f_s = 1 MHz.**

Finally, the convective speeds from all runs were extracted, as described in the previous section, and the results are plotted as open red circles in Fig. 9. Individual experimental realizations agree with each other quite well, giving an averaged convective speed of 942 m/s or approximately 0.88 of the freestream speed, U_∞. Convective speeds for other Mach numbers from [7] are also plotted for the comparison. The convective speed monotonically increases with the Mach number, from $0.82U_\infty$ at subsonic speeds to $0.95U_\infty$ at M = 5.8. However, the convective speed for M = 8 breaks this trend and decreases down to $0.88U_\infty$. The exact reason for this trend is not clear at this moment and currently under investigation.

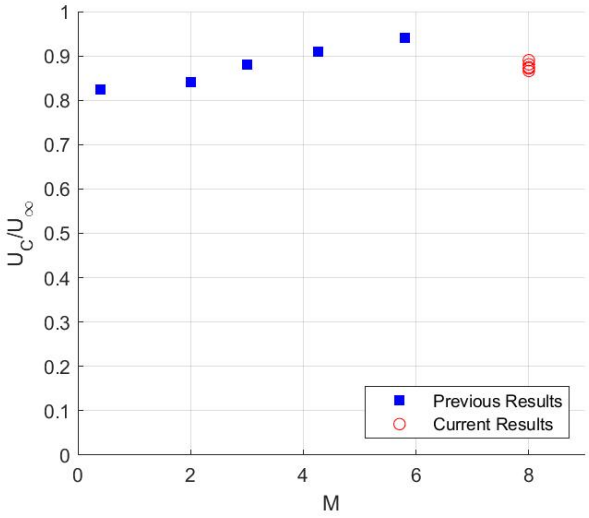

Fig. 9. Convective speeds, normalized by the freestream speed, U_∞, for the current experiments and from previous experiments from [7]**.**

C. 2-D Wavefront Results

Two representative wavefront images from Run 3 are shown in Fig. 10. The additional lenslets along the spanwise direction allow for a reconstruction of the wavefronts from the measured deflection angles using Southwell's method [13]. Instantaneous tip/tilt were removed from each wavefront, as discussed before. As the aperture is only Ap = 15 mm, compared to the boundary layer thickness of δ = 45 mm, only small structures can be observed in Fig. 10. Note that the wavefront spatial peak-to-valley variations are less than 50 nm, indicating a weak aero-optical signal.

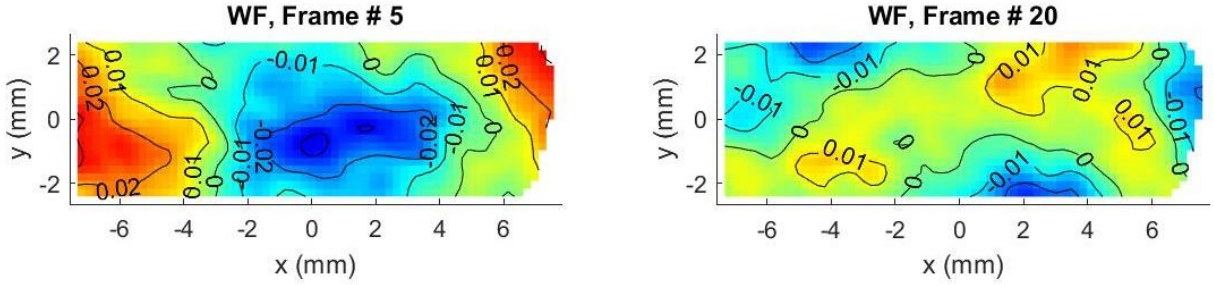

Fig. 10. Representative wavefronts from Run 3. Contour lines are in microns.

As discussed earlier, removing piston and tip/tilt components effectively reduces the overall level of aero-optical distortions, and, as a result, OPD_{rms} depends on the aperture size. This effect can be expressed in terms of the aperture function, $G_A(Ap)$,

$$G_A(Ap) = OPD_{rms}(Ap)/OPD_{rms} \tag{6}$$

where OPD_{rms} is the level of aero-optical distortions for sufficiently large apertures. The transfer functions for turbulent boundary layers for different Mach numbers from [7] are presented in Fig. 11. The transfer functions are

similar for a wide range of Mach numbers, and are monotonically increasing functions, leveling off for apertures on the order of 10δ. Assuming that the transfer function for a M = 8 turbulent boundary layer is similar to those presented in Fig. 11 for Ap/δ = 0.33, the transfer function was estimated to be $G_A \approx 0.22$. Using Eq. 6, OPD_{rms} extracted from Runs 3, 6 and 9 were used to compensate for the aperture effects and to estimate the true OPD_{rms}.

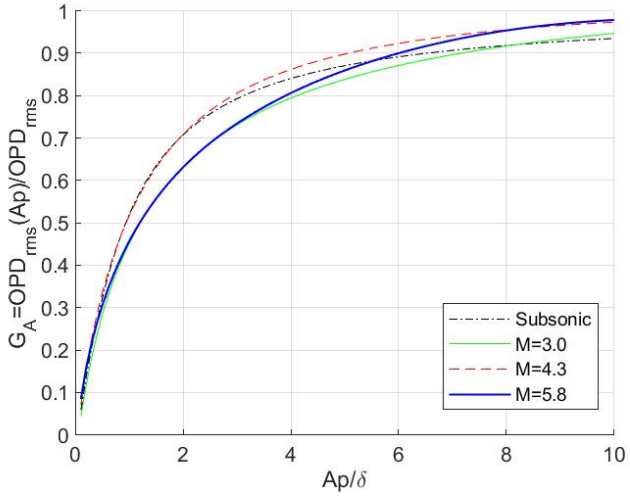

Fig. 11. The aperture function, $G_A(Ap/\delta)$, for a wide range of Mach numbers up to M = 5.8. Adapted from [7] with permission of the American Institute of Aeronautics and Astronautics.

D. Model Comparisons

The theoretical model proposed in [4, 5] states that $OPD_{rms} = F(M_\infty)K_{GD}\rho_\infty M_\infty^2 \delta (C_f)^{1/2}$, where $F(M_\infty)$ is only a function of the freestream Mach number. A comparison of the aero-optical distortion from the de-aliased deflection angle spectra, the aperture-corrected wavefronts, and the theoretical model is shown in Fig. 12. The model and the previous experimental results from [7] are also plotted for comparison. While the results from the deflection angles and 2-D wavefronts are close to each other, OPD_{rms} from the deflection angle spectra are consistently lower than OPD_{rms} values from aperture-corrected 2-D wavefronts. Recall that a low-pass filter was applied to remove the vibration-contaminated lower range of the deflection angle spectra. In doing so, aero-optical components present in this range were also removed from the spectra and the resulting OPD_{rms} values tend to slightly underestimate the true values of aero-optical distortions.

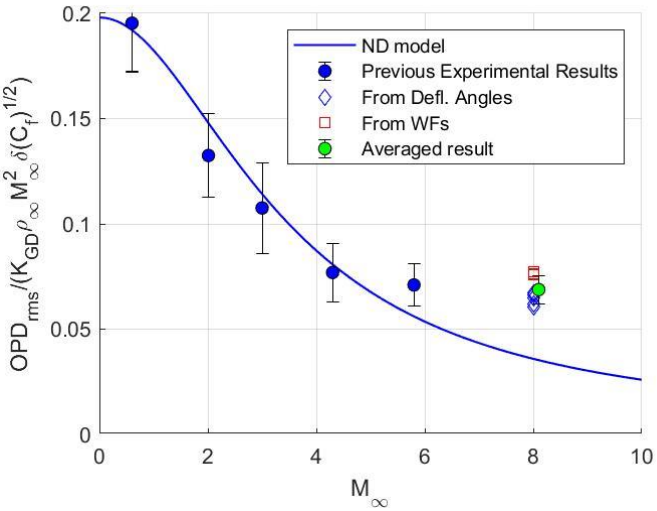

Fig. 12. Normalized levels of OPD_{rms} computed using de-aliased deflection angle spectra and aperture corrected wavefronts, and the averaged result with estimated error bars. Normalized levels of OPD_{rms} at different Mach numbers from [7] and the theoretical model from [4, 5] are plotted for comparison.

The estimated OPD_{rms} are consistently higher, by a factor of two, than the model prediction. The normalized aero-optical distortions begin to plateau near a value F = 0.075 for Mach numbers above 5. The deviation from the model prediction is expected, as assumptions such as the strong Reynolds analogy used to develop the model become increasingly invalid for M > 3. These assumptions are under investigation to extend the model to higher Mach numbers [17]. Also, other aero-optical sources, such as acoustic radiation from hypersonic turbulent boundary layers, might be responsible for higher than predicted values of OPD_{rms}.

Conclusions

Aero-optical measurements of turbulent boundary layers on the wall of a Mach 8 wind tunnel were conducted using a double-pass Shack-Hartmann wavefront sensor. Deflection angles were recorded at different sampling rates and spatial resolutions, ranging from two-dimensional wavefronts sampled at 113 kHz to one-dimensional slices at 1 MHz. A novel de-aliasing algorithm, based on the 2-D Fourier transform, is proposed to isolate the convective-only component of the deflection angle spectra. It is shown that the algorithm can extract correct spectra even for low sampling frequencies of 393 kHz, and the algorithm extracts useful spectrum information beyond the sampling frequency. The de-aliased deflection angle spectra were used to compute the convective speeds of the aero-optical structures and the resulting optical distortion. Two-dimensional wavefronts were corrected for aperture affects and provide an alternative means for estimating the level of aero-optical distortions. Comparison of the deflection-angle spectra with those at lower Mach numbers shows that the spatial properties of the underlying aero-optical structures do not significantly vary over a wide range of Mach numbers, with a consistent peak at a scale approximately equal to the boundary layer thickness. The average convective speed of the aero-optical structures was found to about 0.88 of the freestream speed, which is lower than the convective speeds reported previously at lower supersonic Mach numbers. Comparison of the measured aero-optical levels with an existing theoretical model reveals that the experimental results are higher than the model prediction by almost a factor of two at the reported Mach number. The presented results can used to estimate aero-optical levels of turbulent boundary layers at high supersonic and hypersonic speeds and to validate numerical simulations of aero-optical distortions at these speeds.

Acknowledgments

The authors gratefully acknowledge the support of the Laboratory Directed Research and Development (LDRD) program at Sandia National Laboratories. This paper describes objective technical results and analysis. Any subjective views or opinions that might be expressed in the paper do not necessarily represent the views of the U.S. Department of Energy or the United States Government. Sandia National Laboratories is a multimission laboratory managed and operated by National Technology & Engineering Solutions of Sandia, LLC, a wholly owned subsidiary of Honeywell International Inc., for the U.S. Department of Energy's National Nuclear Security Administration under contract DE-NA0003525.

References

[1] W. Merzkirch, Flow Visualization, Academic Press, 2012.

[2] M. Wang, A. Mani and S. Gordeyev, "Physics and Computation of Aero-Optics," *Annual Review of Fluid Mechanics,* vol. 44, pp. 299-321, 2012.

[3] C. Wyckham and A. Smits, "Aero-optic distortion in transonic and hypersonic turbulent boundary layers," *AIAA Journal,* vol. 47, no. 9, pp. 2158-2168, 2009.

[4] S. Gordeyev, A. Smith, J. Cress and E. Jumper, "Experimental studies of aero-optical properties of subsonic turbulent boundary layers," *Journal of Fluid Mechanics,* vol. 740, pp. 214-253, 2014.

[5] S. Gordeyev, J. A. Cress, A. Smith and E. J. Jumper, "Aero-optical measurements in a subsonic, turbulent boundary layer with non-adiabatic walls," *Physics of Fluids,* vol. 27, no. 4, pp. 1-17, 2015.

[6] S. Gordeyev, R. M. Rennie, A. B. Cain and T. E. Hayden, "Aero-optical measurements of high-Mach supersonic boundary layers," in *46th AIAA Plasmadynamics and Lasers Conference*, Dallas, 2015.

[7] S. Gordeyev and T. Juliano, "Optical characterization of nozzle-wall Mach-6 boundary layers," in *54th AIAA Aerospace Sciences Meeting*, San Diego, 2016.

[8] S. Gordeyev and T. Juliano, "Optical Measurements of Transitional Events in a Mach-6 Boundary Layer," *AIAA Journal,* vol. 55, no. 11, pp. 3629-3639, 2017.

[9] M. Winter, R. Green, C. Borchetta, E. Josyula, J. Hayes, J. Jewell and B. Hagen, "Experimental investigation of image distortion in a Mach 6 hypersonic flow," in *2018 Aerodynamic Measurement Technology and Ground Testing Conference*, Atlanta, 2018.

[10] S. Lee, M. Jeong, I. Jeung, H. J. Lee and J. K. Lee, "Aero-optical measurement in shock wave of hypersonic flow field," in *30th International Symposium on Shock Waves*, Tel Aviv, 2017.

[11] K. M. Casper, Hypersonic Wind-Tunnel Measurements of Boundary-Layer Pressure Fluctuations, Master's Thesis, Purdue University, 2009.

[12] J. A. Smith, L. J. DeChant, K. M. Casper, M. Mesh and R. V. Field, Jr., "Comparison of a Turbulent Boundary Layer Pressure Fluctuation Model to Hypersonic Cone Measurements," in *34th AIAA Applied Aerodynamics Conference* , Washington, D.C., 2016.

[13] W. H. Southwell, "Wave-front estimation from wave-front slope measurements," *Journal of the Optical Society of America*, vol. 70, no. 8, pp. 998-1006, 1980.

[14] J. Siegenthaler, S. Gordeyev and E. Jumper, "Shear Layers and Aperture Effects for Aero-Optics," in *AIAA Paper 2005-4772*, 2005.

[15] S. Gordeyev and M. Kalensky, "Effects of Engine Acoustic Waves On Aero-Optical Environment In Subsonic Flight," *AIAA Journal*, vol. 58, no. 12, pp. 5306-5317, 2020.

[16] J. S. Bendat and A. G. Piersol, Random Data, Wiley, 2010.

[17] N. E. Miller, D. R. Guildenbecher and K. P. Lynch, "Aero-Optical Distortions of Turbulent Boundary Layers: DNS up to Mach 8," in *AIAA Aviation 2021*, 2021.